

Enhanced Oxidation Resistance of Ultrafine-Grain Microstructure AlCoCrFeNi High Entropy Alloy

Mayank Garg, Harpreet S. Grewal, Ram K. Sharma, and Harpreet S. Arora*

Cite This: *ACS Omega* 2022, 7, 12589–12600

Read Online

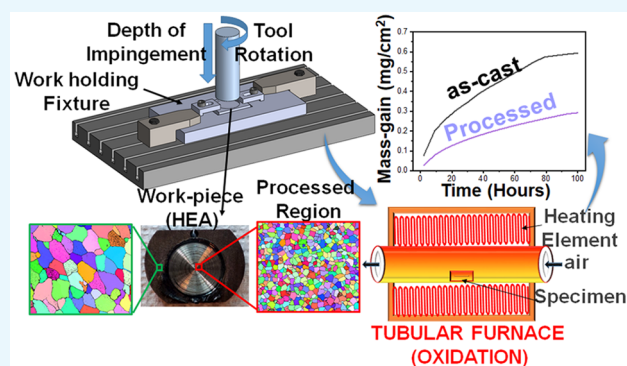
ACCESS |

Metrics & More

Article Recommendations

Supporting Information

ABSTRACT: This work investigates the effect of ultrafine-grain microstructure on the oxidation behavior of AlCoCrFeNi high entropy alloy (HEA). The ultrafine-grain microstructure is obtained using stationary friction processing performed at two different rotational speeds, 400 and 1800 rpm, for 5 min duration. Processed samples demonstrate high depth of refinement (DOR) and ultrafine grain size ($0.43\text{--}1\ \mu\text{m}$) at high rotational speeds along with significant phase transformations from BCC/B2 to FCC microstructure. Further, surface free energy of the ultrafine-grain microstructure is enhanced up to 35%. Oxidation kinetics of the ultrafine-grained sample is decelerated up to 12–48% in a temperature range of $850\text{--}1050\ \text{°C}$ for a duration of 100 h. Chromia and alumina were the predominant oxides formed in almost all the samples oxidized at elevated temperature. In addition, spinel $\text{Co}(\text{Cr,Fe})_2\text{O}_4/\text{Fe}(\text{Co,Cr})_2\text{O}_4$ formation is also detected in the unprocessed oxidized samples. Processed samples rich in grain boundaries (GBs) promote internal oxidation to form Al-rich inner oxides. The enhanced oxidation resistance of the processed samples is attributed to the microstructural refinement and homogenization resulting in the formation of protective chromia followed by Al-rich inner oxides.



1. INTRODUCTION

In the energy sector, there is an increased worldwide demand for power generation owing to rapid population growth.¹ Thermal power generation using a combined cycle is one of the most useful energy resources and can enhance net up to ~60% efficiency for the system as compared to a conventional thermal power cycle.² Gas-fired energy generation systems are particularly important as these can produce power in a small space and play a vital role in supply chain management for regulating the electric energy in power grids. In a gas turbine including in the aerospace industry, increasing the maximum operating temperature permits improvement of the thermal to mechanical energy conversion efficiency, providing an opportunity for cost reduction of the technology.³ However, gas turbine blades, such as nozzle guide vanes and rotor blades, deteriorate over time owing to high temperature corrosion and oxidation, hence becoming thinner and shorter. The cost of frequently replacing the degraded components has a substantial impact on the power plant's economy. Since the sustainability of the turbine blade at maximum operating temperature is a key factor influencing the economic viability of the engine performance, there have been increasing efforts to increase the useful life cycle of components subjected to thermal exposure. In that context, the selection of an appropriate material with outstanding surface properties against oxidation is crucial. Typically, the high temperature components in power plants and the aerospace industry are

made of superalloys. It is well-known that superalloys exhibit a better combination of mechanical properties, such as resistance to thermal fatigue and creep and corrosion resistance at moderate temperatures ($800\text{--}900\ \text{°C}$) only.⁴ The need for high temperature structural materials is steadily increasing, principally driven by the aerospace industry. Surfaces of turbine blades are exposed to exceedingly high temperature, which results in significant material loss over a period of time owing to high temperature oxidation. Improvements in superalloy technology can achieve only relatively modest increases in operating temperatures while the use of improved active component cooling could consume so much energy that the expected gain in engine performance would be significantly reduced.⁵ Hence, thermal insulation is provided on the surface of superalloy components via thermal barrier coatings (TBCs). At high temperature, interdiffusion between Al-rich bond coat and substrate can produce new phases, and O_2 penetration in the porous TBC and bond coat surface leads to oxide scale growth. The phase transitions result in volumetric changes,

Received: October 27, 2021

Accepted: March 25, 2022

Published: April 7, 2022



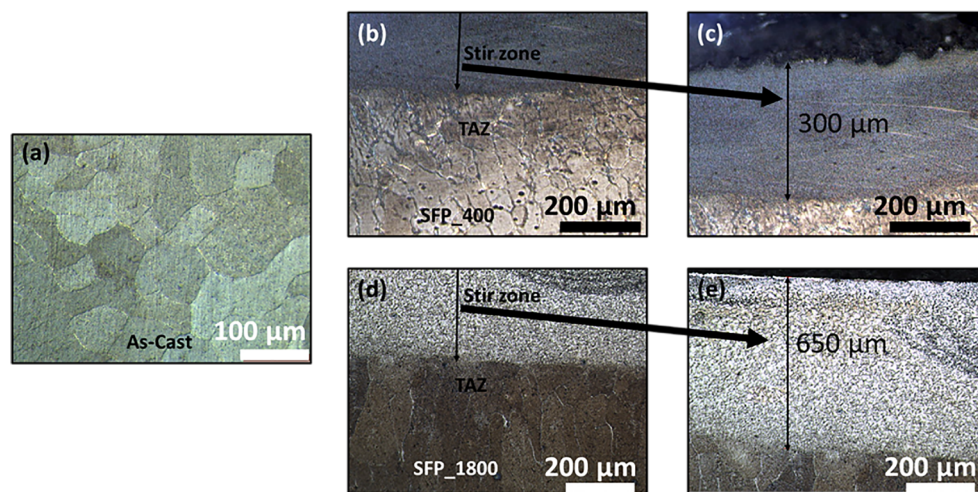


Figure 1. Optical microscope images of (a) as-cast HEA. Cross section of (b) SFP_400, (c) enlarged stir region of SFP_400, (d) SFP_1800 sample, and (e) enlarged stir region of SFP_1800 sample.

resulting in interfacial disruption between the TBC and the underlying oxide scale. This in turn leads to mechanical failure of the TBC, subsequent overheating of the substrate metal, and component failure. The use of superalloys without TBCs is not practiced owing to the rapid deterioration of their mechanical characteristics at high temperatures. Thus, there is a need to develop advanced materials with superior surface oxidation resistance and improved mechanical properties at high temperature.

High entropy alloys (HEAs) represent an emerging class of advanced materials for high temperature applications owing to their promising mechanical properties, namely, outstanding structural strength,⁶ high hardness,^{6b,7} enhanced fracture toughness,⁸ prominent fatigue resistance,⁹ and remarkable oxidation and corrosion resistance.¹⁰ The oxidation behavior of HEAs has been extensively reported. Kim et al.¹¹ examined the oxidation behavior of a Cr–Mn–Fe–Co–Ni HEA system for a duration of 24 h at three different temperatures, 900, 1000, and 1100 °C, revealing mass gain of 1.76, 4.45, and 9.08 mg/cm², respectively. Nong et al.¹² studied the high temperature oxidation behavior of AlCrFeNiTiMn_x (where $x = 0$ and 0.5) HEAs at 900 °C for 100 h and probed the poor oxidation resistance of Mn containing alloys, which was attributed to the adverse effect of Mn-rich oxides. The cumulative mass gain (CMG) of Mn-free and Mn-containing alloys was 6.9 mg/cm² and 8.7 mg/cm², respectively. The high temperature oxidation resistance of the HEAs depends strongly on the oxides being formed during the reactions. Al₂O₃, Cr₂O₃, and SiO₂ are found as protective oxide scales in high temperature oxidation environments. Chen et al.¹³ investigated the effect of Si (0.3 atom %) content on the oxidation behavior of the Al_{0.6}CrFeCoNi HEA and found that the oxidation kinetics of the Si-containing HEA was lower than that of the Al_{0.6}CrFeCoNi HEA at lower temperatures (800 and 900 °C) but became inferior compared to Al_{0.6}CrFeCoNi at the higher temperature of 1000 °C. Lu et al.¹⁴ reported the effect of Al content on the oxidation behavior of Y/Hf-doped Al_xCoCrFeNi ($x = 0.7, 1, 1.3$) high-entropy alloys. Al_{0.7}CoCrFeNi showed the lowest oxidation resistance owing to the formation of an outer spinel layer with an inner Al₂O₃ layer, followed by AlCoCrFeNi due to the formation of

protective Al₂O₃ scale and Al_{1.3}CoCrFeNi exhibiting the highest resistance to oxidation.

While the major focus of prior studies has been on the development of new alloy systems, there are only a few studies on limiting the high temperature oxidation via tailoring the material's microstructure. Surface deformation techniques including surface mechanical attrition treatment,¹⁵ shot peening,¹⁶ microwave processing,¹⁷ and ultrasonic treatment¹⁸ have been utilized to obtain fine-grain microstructure, and subsequently its effect on oxidation behavior was investigated. Similarly, ultrasonic nanocrystal surface modification (UNSM)-assisted thermal oxidation behavior of Ti₆Al₄V alloy was investigated.¹⁸ UNSM gives rise to a significant number of defects and grain refinements by introducing a low amplitude, high frequency vibration of the WC-tip superimposed on the static load. UNSM treated alloy exhibited high adsorption and reaction capabilities with oxygen at 500 and 600 °C. Benafia et al.¹⁹ examined the influence of surface mechanical attrition treatment (SMAT) on the oxidation behavior of 316L stainless steel. The SMAT-assisted sample showed the beneficial effects on the oxidation resistance of the 316L steel at high temperatures owing to the preferential growth of chromia in the SMAT samples. Kanjer et al.¹⁶ reported improved high temperature oxidation resistance of pure Ti after shot peening. The increase in grain boundary density for the nanostructured sample enhanced the N₂ short circuit diffusion paths, which promoted the formation of a nitrogen-rich layer that limits the diffusion of O₂ into the metal. Khanna et al.²⁰ studied the oxidation behavior of 2¹/₄Cr–1Mo steel after cold rolling and reported enhanced oxidation resistance of the cold worked steel samples at high temperatures. Cr diffuses faster toward the surface owing to the increased defect concentration in the cold-worked alloy, and the higher concentration of Cr thus available leads to formation of Cr-rich oxides and reduces the oxidation kinetics.

It is worth mentioning that all the prior studies on microstructural refinement and the oxidation behavior of the resulting materials were limited to conventional structural materials only. To the best of the authors' knowledge, there has been no study on achieving remarkable oxidation resistance in HEAs through microstructural refinement. In the current work, microstructural refinement of the AlCoCr–

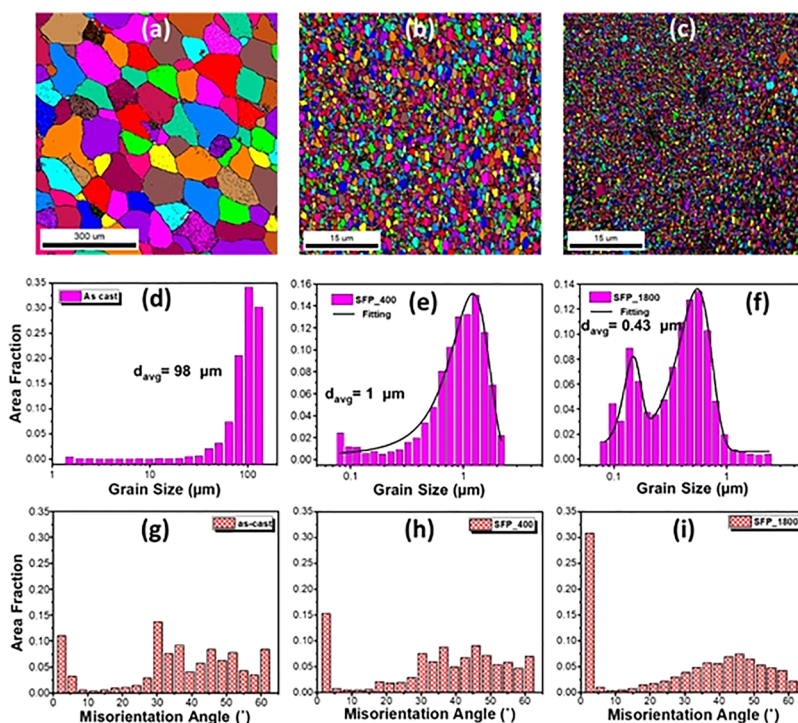


Figure 2. EBSD map for (a) as-cast and (b) SFP_400 and (c) SFP_1800 processed samples. Grain size distribution of (d) as-cast and (e) SFP_400 and (f) SFP_1800 processed samples. Misorientation angle chart for (g) as-cast and (h) SFP_400 and (i) SFP_1800 processed samples.

FeNi HEA was accomplished via severe surface deformation using stationary friction processing (SFP). The processing resulted in ultrafine-grain structure with a significant fraction of nanograins in the as-cast HEA along with significant elemental homogenization. The processed HEA samples demonstrated exceptional oxidation resistance, and the reported mass gain values are among the lowest for the investigated HEA. The remarkable performance of the processed HEAs was attributed to the formation of an intact, dense, uniformly distributed oxide scale, favored by large grain boundary density, higher surface free energy, and uniform elemental distribution.

2. RESULTS AND DISCUSSION

2.1. Microstructure. An optical image of the as-cast HEA is shown in Figure 1a, while the cross-section optical images of both processed samples are shown in Figure 1b–e. The as-cast

Table 1. Test Liquids for Contact Angle Measurement

liquid	σ_i^p (mJ/m ²)	σ_i^D (mJ/m ²)	σ_i (mJ/m ²)
water ($i = 1$) ²⁸	51	21.8	72.8
ethanol ($i = 2$) ²⁹	2.6	18.8	21.4

Table 2. Test Samples for Surface Free Energy

sample	R_a (μm)	θ_1 (deg)	θ_2 (deg)	σ_s^D (mJ/m ²)	σ_s^p (mJ/m ²)	σ_s (mJ/m ²)
as-cast	5.48	40	17	5.08	56.67	61.75
SFP_400	5.35	16	3	3.65	76.53	80.17
SFP_1800	5.63	7	1	3.37	80.12	83.49

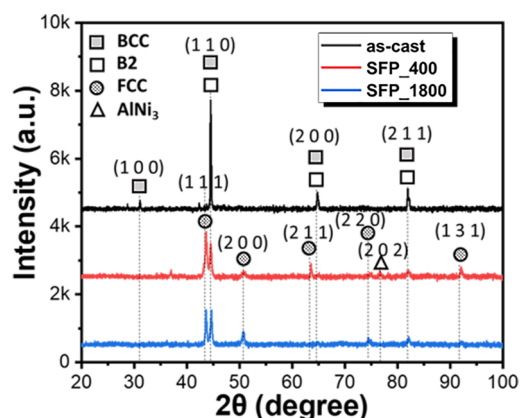


Figure 3. XRD spectra of as-cast, SFP_400, and SFP_1800 samples before oxidation.

HEA showed coarse grains with an average grain size of nearly 100 μm. In contrast, both the SFP samples show a highly refined stir zone, and the grain size could not be obtained from the optical images. The depth of refinement (DOR) varies from 300 to 650 μm for the SFP_400 and SFP_1800 sample, respectively. The increment in DOR with rotational speed is likely due to the thick column of plastically deformed zone during processing at higher rotation speed. The grains of processed samples below the refined zone appear to be elongated, which is caused by the effect of shearing action and corresponds to the thermomechanical affected zone (TMAZ). Figure S1 shows the temperature profile acquired during the SFP at two different rotational speeds. At 400 rpm, the average temperature was nearly ~280 °C, while it increased up to ~760 °C at 1800 rpm. High temperature at higher rotational speed favors the material flow through thermal softening and leads to deeper DOR.

Figure 2 shows the electron backscattered diffraction (EBSD) maps, grain size distribution, and misorientation angle chart of the as-cast and processed samples. In line with optical images, EBSD analysis also showed coarse grain

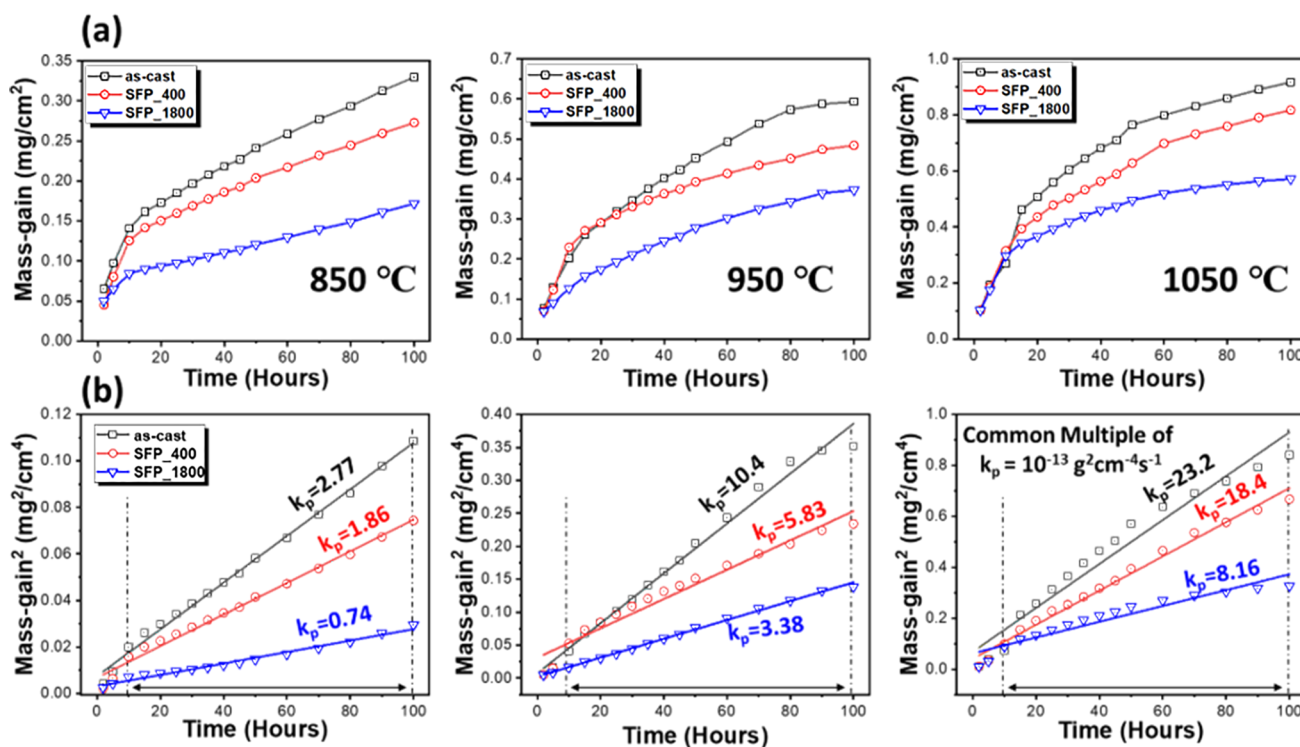


Figure 4. (a) Cumulative mass gain curves and (b) parabolic mass gain curves for as-cast and both the processed samples at three temperatures 850, 950, and 1050 °C.

Table 3. Oxidation Rate Constants Calculated from the Curves Shown in Figure 4

alloys	t_1 [h]	t_2 [h]	k_i/k_p	T (°C)		
				850	950	1050
as-cast	1	10	k_i [$\text{g}\cdot\text{cm}^{-2}\cdot\text{s}^{-1}$]	3.00×10^{-9}	5.01×10^{-9}	6.61×10^{-9}
	10	100	k_p [$\text{g}^2\cdot\text{cm}^{-4}\cdot\text{s}^{-1}$]	2.77×10^{-13}	10.4×10^{-13}	23.2×10^{-13}
SFP_400	1	10	k_i [$\text{g}\cdot\text{cm}^{-2}\cdot\text{s}^{-1}$]	3.18×10^{-9}	6.32×10^{-9}	8.42×10^{-9}
	10	100	k_p [$\text{g}^2\cdot\text{cm}^{-4}\cdot\text{s}^{-1}$]	1.86×10^{-13}	5.83×10^{-13}	18.4×10^{-13}
SFP_1800	1	10	k_i [$\text{g}\cdot\text{cm}^{-2}\cdot\text{s}^{-1}$]	1.37×10^{-9}	2.64×10^{-9}	6.25×10^{-9}
	10	100	k_p [$\text{g}^2\cdot\text{cm}^{-4}\cdot\text{s}^{-1}$]	0.74×10^{-13}	3.38×10^{-13}	8.16×10^{-13}

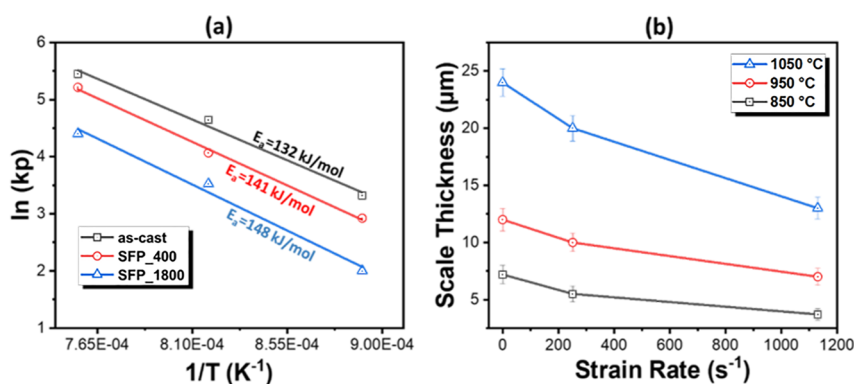


Figure 5. (a) Activation energy of as-cast, SFP_400, and SFP_1800 samples and (b) variation of scale thickness with strain rate.

microstructure for the as-cast alloy with an average grain size of 98 μm. The average grain size of all three samples is calculated using the areal average method. The color mapping shows the unique color of each individual grain. The number of grains found in as-cast, SFP_400, and SFP_1800 samples during the EBSD analysis were 2716, 26773, and 66853, respectively. Both processed samples showed remarkably refined microstructure. The fitting of grain size distribution of processed

samples is performed using a Gaussian function (Figure 2) given as follows:

$$y = y_0 + \left(\frac{A}{w\sqrt{\pi/2}} \right) e^{-2(x-x_c)^2/w^2}$$

where y and x represents area fraction and grain size, respectively. In addition, the fitting parameters y_0 , x_c , w , and

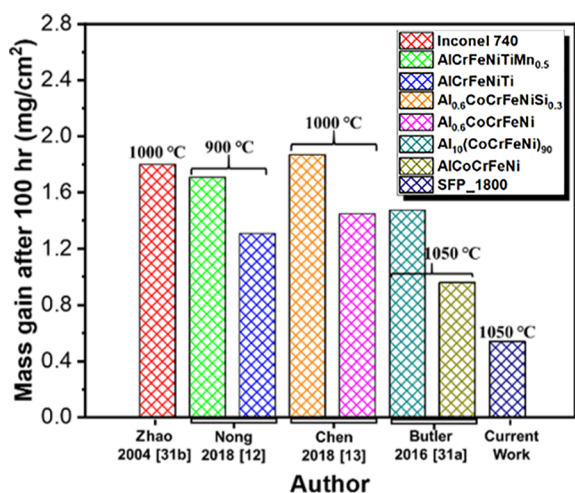


Figure 6. Comparison of mass-gain of SFP_1800 sample with other alloy systems for high temperature oxidation.

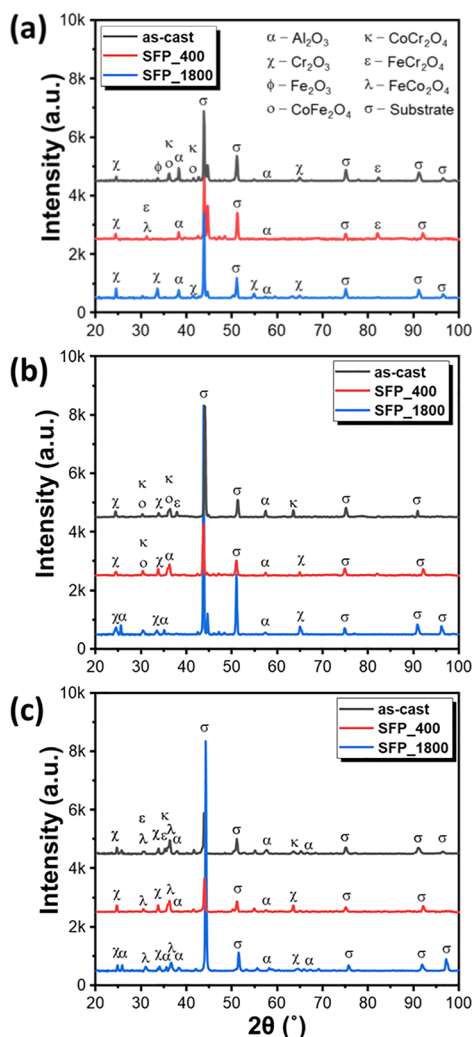


Figure 7. XRD spectra of as-cast and SFP_400 and SFP_1800 processed samples after oxidation at temperatures (a) 850 °C, (b) 950 °C, and (c) 1050 °C.

A denote the offset, center, width, and area under the fitting curve, respectively. The grain size distribution of the SFP_400 sample demonstrates a unimodal distribution with an average

grain size of 1 μm , while that of the SFP_1800 sample demonstrates bimodal distribution with an average grain size of 0.43 μm . The fitting of the data was performed only for one mode in the SFP_400 sample and for two modes in the SFP_1800 sample. The fitting parameters for both distributions are given in the Supporting Information (Table S1). Thus, the higher tool rotational speed of 1800 rpm resulted in highly refined sub-micrometer grain structure with a significant fraction ($\sim 54\%$) of nanograins. Besides this, the SFP_1800 sample shows three contributions to the average grain size, of which two peaks indicate two major contributions owing to the formation of bimodal grain microstructure as evident from earlier studies as well.²¹ The calculations for grain size distribution and misorientation angle determination were performed using TSL OIM Analysis 8.0 software. The fraction of high angle grain boundaries (HAGBs, $\theta > 15^\circ$) is reduced from nearly 87% for the as-cast sample to $\sim 82\%$ and 66% for the SFP_400 and SFP_1800 samples, respectively. The evolution of refined microstructure during processing is attributed to dynamic recrystallization, which is a function of strain-rate and peak temperature. The strain-rate ($\dot{\epsilon}$) during processing was obtained using the expression²² $\dot{\epsilon} = R_m(2\pi r/l)$, where r is the effective radius of the processed zone, l is the effective depth of the processed zone, and R_m is the materials flow rate, which is taken as half the rotational speed in the present study.²² The strain rate was found to vary from 251.31 s^{-1} for the SFP_400 sample to 1130.90 s^{-1} for the SFP_1800 sample. The peak temperature during processing was measured to be ~ 320 °C and ~ 780 °C for SFP_400 and SFP_1800 samples, respectively. The combined effect of strain rate and peak temperature can be expressed using the Zener–Hollomon parameter (Z), which is given by the following equation:²³ $Z = \dot{\epsilon} e^{Q/(RT)}$, where Q is the activation energy, R is the universal gas constant, and T is the peak temperature during SFP. The recrystallized grain size can be expressed by the relation ($Z \propto 1/\sqrt{d}$) where d is the average grain size. It is evident that the recrystallized grain size is inversely proportional to the Z parameter. Thus, the highly refined grain structure of SFP_1800 sample is attributed to high strain-rate deformation resulting in dynamic recrystallization.

The XRD spectra of the as-cast and both processed samples is shown in Figure 3. The as-cast sample shows BCC/B2 phases whereas both processed samples show FCC phase along with BCC/B2 phases. The evolution of the FCC phase is likely due to BCC/B2 phase transformation into FCC during high strain-rate processing. In HEAs, BCC/B2 to FCC phase transformations have been shown in earlier studies as well.²⁴ The peak intensity of the FCC phase is higher in the SFP_1800 sample as compared to SFP_400 sample, which indicates a higher fraction of phase transformation in SFP_1800. Further, EBSD phase maps (Figure S2) were extracted in order to quantify the phase fraction. The FCC phase transformation obtained in the SFP_400 sample is 38%, while that for SFP_1800 is 55%. The likely reason for the phase transformation is the significant increase in the defect density, namely, dislocation density, point defects, and GB fraction, which increases the system energy during SFP. Other than B2/BCC and FCC phases, an AlNi-rich phase is also observed with a weak peak intensity in the SFP_400 sample. Moreover, X-ray peak profile analysis (XPPA) was performed in order to investigate strain present in the as-cast and processed samples. The instrumental broadening was cor-

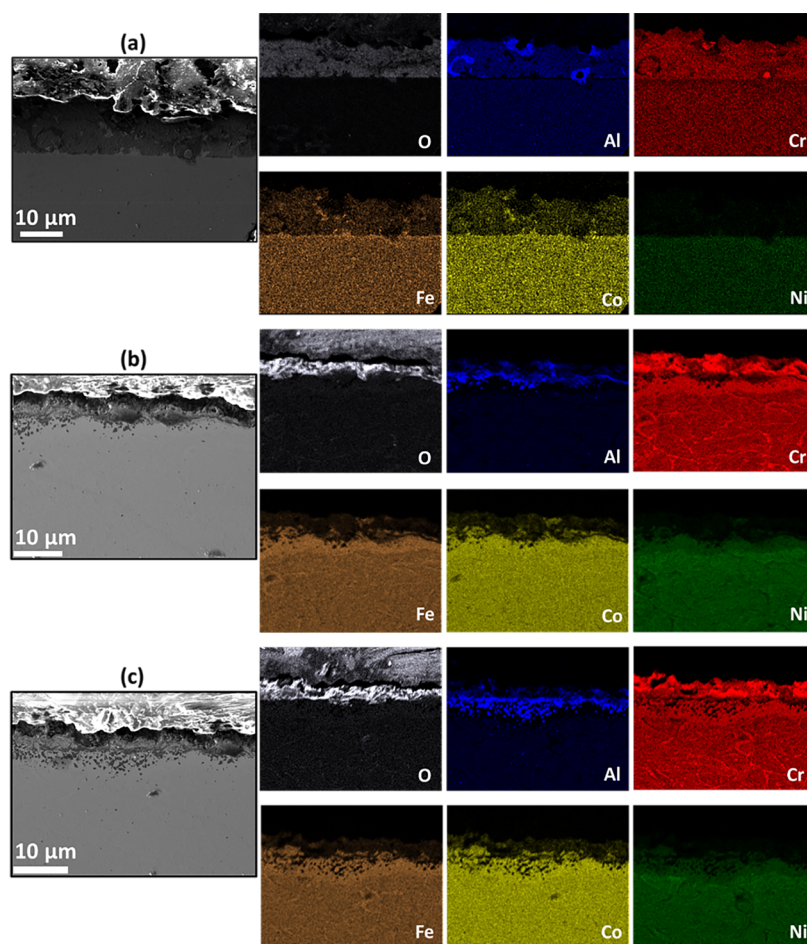


Figure 8. BSE images with EDS analysis of (a) as-cast (b) SFP_400 and (c) SFP_1800 processed sample after oxidation at 850 °C.

rected, corresponding to each diffraction peak of HEA using following formula:

$$\beta_{hkl} = \sqrt{\beta_{hkl}^2(\text{measured}) - \beta_{hkl}^2(\text{instrumental})}$$

According to Williamson–Hall (W–H) analysis,²⁵ $\beta_{hkl} \cos \theta = \varepsilon 4 \sin \theta + \frac{K\lambda}{D}$, where β represents full width at half-maximum (FWHM), θ is half of the diffraction angle, λ is the wavelength of the Cu $K\alpha$ radiation, K is shape factor, D is the crystallite size, and ε is the microstrain. Peak fitting of each spectrum was performed using a Gaussian function to estimate FWHM. Further, the W–H graph was plotted as shown in Figure S3. The slope of the graph represents the value of microstrain. The microstrain values obtained for as-cast, SFP_400, and SFP_1800 were 0.00131, 0.00259, and 0.00674, respectively. Clearly, the microstrain present in the SFP_400 and SFP_1800 samples are ~ 2 and ~ 5 times greater than that of the as-cast sample. Residual stress analysis was performed to estimate the variation of residual stress in as-cast, SFP_400, and SFP_1800 samples as shown in Figure S4. The calculated residual stress (σ_{11}) along the longitudinal direction on the top surface of as-cast, SFP_400, and SFP_1800 samples was ~ 83 MPa, -90 MPa, and -258 MPa, respectively. Hence, it can be seen that the as-cast sample exhibits tensile stress while SFP induces compressive stress and that the intensity of the compressive stress is greater in the sample processed at high strain rate.

2.2. Estimation of Surface Free Energy. The oxidation kinetics and surface chemistry were observed to vary significantly with the alloy processing. To understand this observation, the surface free energy (SFE) of the as-cast and processed samples was estimated through wetting studies. According to Fowkes,²⁶ SFE can be expressed in terms of the dispersive and polar components of surface tension, wherein the surface tension components can be estimated using contact angle measurements. The surface tension for the two different liquids, along with their corresponding polar and dispersive components, are shown in Table 1. Along with this, surface roughness profiles were extracted (Figure S5), and the roughness factor was calculated for each sample (Table 2). The equation for estimating the SFE and its polar and dispersive components is given as

$$\sigma_s = \sigma_s^D + \sigma_s^P \quad (1)$$

$$\sigma_{li}(1 + \cos \theta_i) = 2(\sqrt{\sigma_{li}^D \sigma_s^D} + \sqrt{\sigma_{li}^P \sigma_s^P}) \quad (2)$$

where θ_i denotes the contact angle between the liquid–air interface and the surface, σ_s^D and σ_s^P are dispersive and polar components of the surface free energy of the alloy, respectively, and σ_{li}^D and σ_{li}^P are the dispersive and polar components of the surface tension of the liquid (i), respectively.²⁷

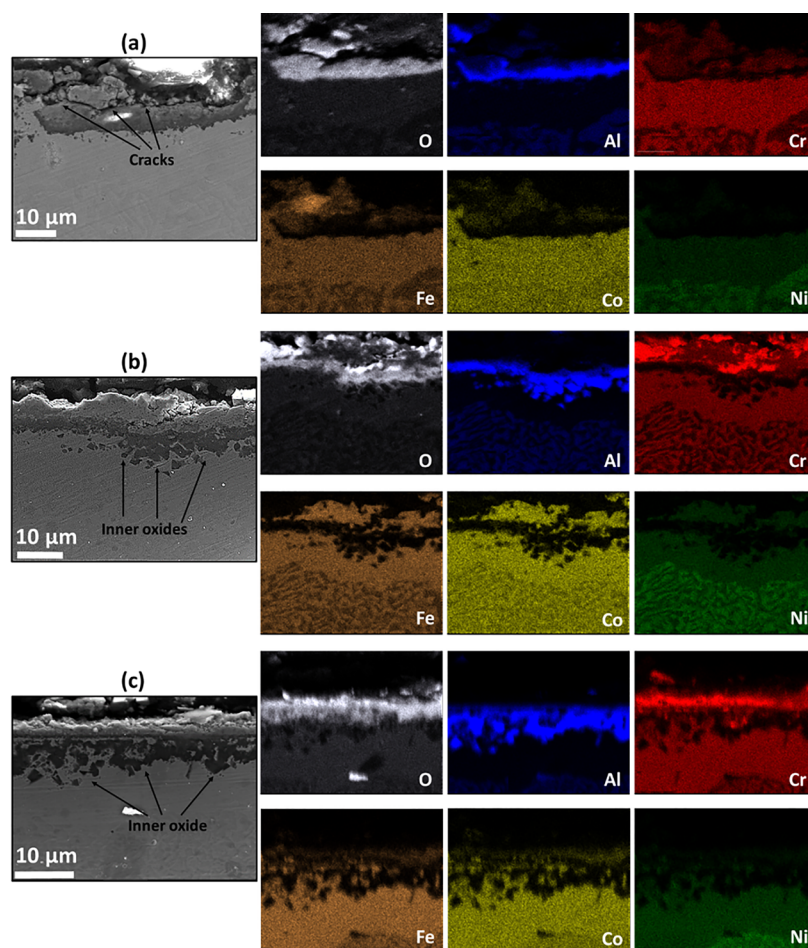


Figure 9. BSE images with EDS analysis of (a) as-cast and (b) SFP_400 and (c) SFP_1800 processed samples after oxidation at 950 °C

$$\sigma_S^D = \frac{\left\{ (1 + \cos \theta_2) \sigma_{12} - \sqrt{\frac{\sigma_{12}^P}{\sigma_{11}^P}} (1 + \cos \theta_1) \sigma_{11} \right\}^2}{\left(2\sqrt{\sigma_{12}^D} - 2\sqrt{\frac{\sigma_{12}^P}{\sigma_{11}^P}} \sigma_{11}^D \right)^2} \quad (3)$$

The subscript 1 denotes water, while the subscript 2 denotes ethanol. The dispersive component of the SFE decreased gradually with the decrease in grain size, while the polar component of the SFE increased. Total SFE of a sample reflects the combined effects of the dispersive and polar components, but the effect of the polar component is dominant over that of the dispersive component. The SFE values of the as-cast, SFP_400, and SFP_1800 samples are 61.75 mJ/m², 80.17 mJ/m², and 83.49 mJ/m², respectively. There is a 29.8% increase in the SFE of the SFP_400 sample and a 35.2% increase in the SFE of the SFP_1800 sample. The increase in surface free energy provides a greater number of favorable sites (grain boundaries) for the chemisorption of O₂ owing to increased reactivity of elements in the alloy system.

2.3. Oxidation Kinetics. The oxidation kinetics for the as-cast and processed samples exposed to elevated temperatures for 100 h is shown in Figure 4. All three samples follow linear oxidation kinetics during the initial 1–10 h duration. Subsequently, all the samples show a steady-state oxidation reaction (SSOR), which follows the parabolic oxidation behavior. In SSOR, the kinetics of oxide growth are governed by the diffusion of ionic species through initially formed oxide

scale. The cumulative mass gain (CMG) for the as-cast, SFP_400 and SFP_1800 samples at 850 °C after 100 h is 0.33, 0.27, and 0.17 mg/cm², respectively. CMG for the same samples at 950 °C is 0.6, 0.48 and 0.37, respectively. Similarly, at 1050 °C, the mass gain values were found to be 0.92, 0.81, and 0.57 mg/cm², respectively. Thus, SFP_400 shows a 12–20% reduction in the oxidation kinetics while SFP_1800 shows a 38–48% reduction as compared to the as-cast sample in the temperature range of 850–1050 °C.

Typically, the reaction kinetics are described by Wagner's parabolic rate law as $(\Delta m)^2 = k_p t + C$, where, Δm is the CMG per unit surface area (mg/cm²), k_p is the parabolic rate constant (mg²·cm⁻⁴·s⁻¹), t is the oxidation time, and C is the constant of integration. The parabolic mass gain curves were plotted as a function of time as shown in Figure 4b. The k_p values were extracted from the slope in the SSOR regime of the parabolic mass gain curve. Table 3 shows the values of linear and parabolic rate constant for all the three samples. The k_p value of the SFP_400 sample is marginally lower than that of the as-cast sample while that for the SFP_1800 sample is considerably lower at a fixed temperature, signifying its excellent oxidation resistance. In addition, it can be seen that parabolic mass gain curves of the as-cast samples at 950 and 1050 °C are deflected slightly from their fitted curves. The oxide layer formed on the as-cast sample includes cracks (discussed in the next section), which causes fluctuations in the oxidation kinetics leading to the nonuniform parabolic mass-gain curve.

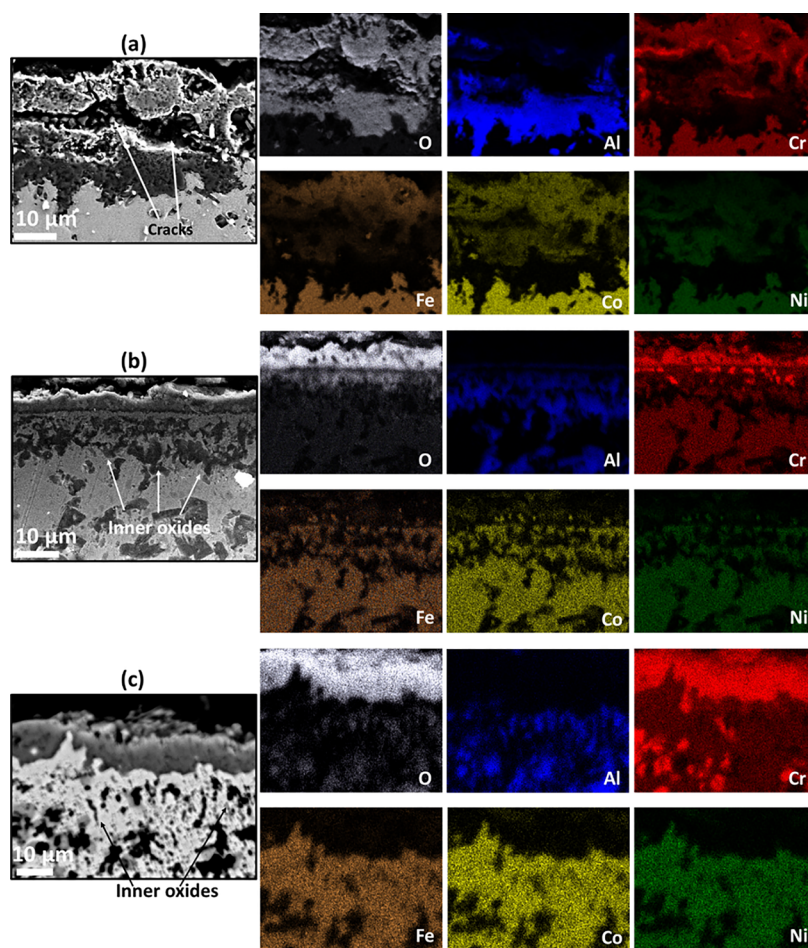


Figure 10. BSE images with EDS analysis of (a) as-cast and (b) SFP_400 and (c) SFP_1800 processed samples after oxidation at 1050 °C.

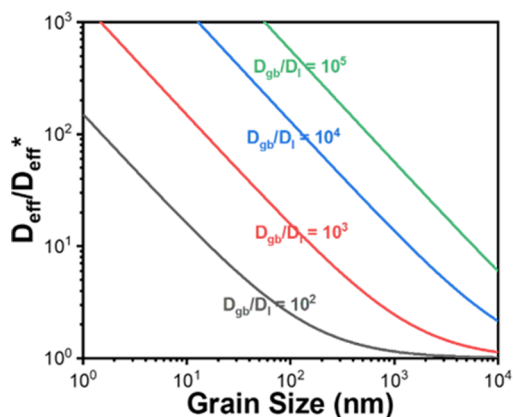


Figure 11. Variation of diffusion coefficient with grain size.

The activation energy of the oxidation can be estimated by regression modeling with the Arrhenius plot. Kofstad³⁰ proposed a convenient way to compute the value of activation energy in a given temperature range. This involves a long-term isothermal oxidation run at three or more different temperatures. Parabolic rate constants, obtained from oxidation kinetics curves, are plotted with respect to reciprocal of temperature. Figure 5a shows the variation of parabolic rate constant with change in temperature. According to the Arrhenius equation, $k_p = k_0 \exp(-E_a/(RT))$, where k_0 is a pre-exponential coefficient, R is the universal gas constant, T is

the temperature of the oxidation process, and E_a is the activation energy. In a diffusion controlled phenomenon, a linear regression model was fitted using Arrhenius curves. The slope of the curve yields the value of $-E_a/R$ in the temperature range of 850–1050 °C, which was utilized to calculate the value of activation energy. The slope of the curves indicates that the activation energy is the lowest value for the as-cast sample while it is highest for the SFP_1800 sample, indicating the high oxidation resistance of the latter. The possible reason for the higher activation energy for the processed samples is the highly stable nature of the thin oxide layer formed on these samples (discussed in the next section). Figures S6–S8 show the thickness of the oxide scale for different samples. Figure 5b plots the oxide scale thickness of the AlCoCrFeNi HEA after 100 h of oxidation as a function of strain rate. The oxide scale thickness was measured using five cross-sectional backscattered secondary electron (BSE) images of the oxide scale. The average value of scale thickness, with error bar showing the standard deviation, was obtained. The scale thickness decreased with the increase in strain rate at a particular testing temperature. Further, the effect of strain rate became more significant at higher testing temperatures. The trend of the curve shows a negative slope, which indicates higher oxidation resistance of the samples processed at higher strain rates. Ultrafine-grain microstructure exhibiting a high fraction of GBs obtained at a high strain rate favors the formation of a Cr-rich scale (initially) and protects the substrate from further oxidation.

The CMG of the ultrafine-grained HEA (SFP_1800) sample was also compared with other advanced structural materials and HEAs,^{12,13,31} and the comparison is shown in Figure 6. The high temperature (900–1050 °C) oxidation resistance of AlCoCrFeNi HEA is higher compared to superalloy (Inconel 740^{31b}) and other HEA systems.^{12,13} The outstanding high temperature oxidation resistance of the equimolar AlCoCrFeNi composition obtained in the current study is of significant importance for high efficiency engineering systems.

2.4. Identification of Oxide Phases. XRD analysis of the surface oxide scales formed after the oxidation runs is presented in Figure 7. All the samples showed the presence of Al₂O₃ and Cr₂O₃ phases. The oxidation products for the as-cast sample oxidized at 850–950 °C consists of CoCr₂O₄, CoFe₂O₄, FeCr₂O₄ spinel, and Fe₂O₃ oxides. At 1050 °C, the as-cast sample exhibits the formation of spinel oxides CoCr₂O₄, FeCr₂O₄, and FeCo₂O₄. In contrast, ultrafine-grained samples primarily showed the formation of Al₂O₃ and Cr₂O₃ in the temperature range of 850–1050 °C. Also, a low intensity peak of FeCr₂O₄/FeCo₂O₄ and CoCr₂O₄/CoFe₂O₄ was found in the SFP_400 sample at temperatures of 850 and 950 °C, respectively. At 1050 °C, a peak of FeCo₂O₄ was detected in the SFP_400 and SFP_1800 samples too. Thus, the as-cast sample is characterized by protective alumina/chromia and nonprotective spinels, while the processed samples showed primarily the protective alumina and chromia with a minor fraction of nonprotective spinels. Moreover, contribution of each oxide phase in all three samples oxidized at three different temperatures is shown in Figure S9.

2.5. Cross section Observation of Oxide Layer. Figures 8–10 show the cross section BSE images of the oxidized samples along with their EDS elemental mapping. The elemental distribution indicates the formation of the mixed oxides in the as-cast sample oxidized at elevated temperatures, 850, 950, and 1050 °C, due to the slow diffusion of elements through GBs owing to the low number of GBs. Ultrafine grain size promotes the diffusion phenomenon owing to the higher number of GBs, which offer adequate diffusion paths for the mobility of ionic species. As-cast sample oxidized at 850 °C exhibits an oxide layer comprising Cr-, Fe-, and Co-rich oxides with a minor amount of Al₂O₃. However, the oxide layer formed on the surface of ultrafine-grained samples oxidized at 850 °C consists of a thin Cr₂O₃ layer followed by aluminum-rich inner oxides. The formation of chromia on the alloy's surface is due to the outward diffusion of Cr ions through GBs,³² while alumina grows at the bottom-most oxide owing to the inward diffusion of O ions.³² The surface of as-cast samples oxidized at 950–1050 °C consists of an alumina layer at the bottom with appropriate fractions of Cr-, Fe-, and Co-rich oxides on the upper part of the scale. The Cr-, Fe-, and Co-rich oxide phases detected as spinel FeCr₂O₄ and Co(Fe,Cr)₂O₄ were also evident from the XRD analysis. These brittle spinels are detrimental as they reduce the protectiveness of the oxide scale and undermine interfacial adhesion.³³ The BSE image of the as-cast alloy reveals a number of cracks (Figures 9a and 10a) propagated within the oxide layer, which allow more O ions to penetrate through the defects. In contrast, both ultrafine-grained samples show a densely packed and well adherent oxide scale in a temperature range of 950–1050 °C. The oxide scale of both the samples is composed of a layered structure with top chromia and aluminum-rich inner oxides. Between these layers, a thin layer of mixed oxides of Cr, Fe,

and Co exists for the SFP_400 sample oxidized at 950 °C, which was confirmed as spinel Co(Fe,Cr)₂O₄ oxide phases from the XRD spectra. Thus, only a few spinel oxides were detected in the ultrafine-grained oxidized samples. The likely reason for the lack of spinel species in the processed samples is the high surface free energy, which suppresses the formation of spinel oxides. Typically, the ultrafine-grained samples with high surface free energy sites are prone to oxygen attack at elevated temperatures owing to the defects and high GBs. According to selective oxidation theory, a large number of GBs in ultrafine-grain microstructure can significantly enhance the diffusional paths for Cr out-flux and hence favors the formation of Cr₂O₃ on the surface of the alloy. In addition, ultrafine-grained samples oxidized at 950 and 1050 °C show a considerable internal oxidation zone (IOZ). EDS maps show the presence of Al-rich oxides in the IOZ as shown in Figures 9 and 10.

The order of formation of various metal oxides is governed by their thermodynamic properties, given by Gibbs free energy at a specific temperature. Al₂O₃ mainly forms as the bottom most oxide layer, due to its highest thermodynamic energy of formation (−903.88 kJ/mol of O₂ at 850 °C) calculated using FactsageEdu73 software. Chromia, with the lowest standard free energy (−574.26 kJ/mol of O₂ at 850 °C), forms the topmost oxide layer for the ultrafine-grained samples. Inner oxides are more likely to form in samples processed at high strain rate, since short circuit diffusion channels and high SFE sites are provided by the high intensity GBs present in the ultrafine-grained samples.³⁴ These channels aid the inward flux of O ions to react with the metallic ions and form the internal oxides. The poor oxidation behavior of the as-cast samples is due to the formation of a nonadherent mixed oxide layer (spinel) above the alumina scale owing to the low diffusion of elements through GBs, which fails to restrict the accumulation of cations (M⁺) and anions (O^{2−}) as reported in few previous studies as well.³⁵ In contrast, the formation of the dense protective Cr₂O₃ layer followed by Al₂O₃ inner oxide layered structure in the processed samples is favored by ultrafine-grain microstructure. Formation of this dense layered structure act as a barrier for the oxidation process to proceed further, which provide high oxidation resistance to the processed samples.

The cross-sectional analysis showed different oxide chemistry for the as-cast and processed samples. The difference in oxide chemistry can be explained based on the microstructure evolution after processing. The ultrafine grain size of SFP_400 and SFP_1800 samples is significantly smaller than that of the as-cast sample as shown in Figure 2e,f. The increased number of GBs will influence the diffusion coefficient, which, consequently, affects the oxidation kinetics. An effective diffusion coefficient (*D*), which is a sum of GB diffusion and lattice diffusion coefficient, was analyzed to explain this:³⁶

$$D = \frac{3\delta}{d} D_{\text{gb}} + D_1 \quad (4)$$

where *D*_{gb} and *D*₁ are the diffusion coefficients along the GBs and lattice and δ and *d* denote the GB width and grain size, respectively. As a reference, the effective diffusion coefficient, *D*^{*}, for coarse grains (*d* = 98 μm) was chosen, and the ratio *D*/*D*^{*} was used to represent effective diffusion coefficient as a function of average grain size. Grain size dependence of the effective diffusion coefficient is plotted as shown in Figure 11 using eq 4 and shows the increase in effective diffusion coefficient with the decrease in the grain size. The decrease in grain size is attributed to the enhanced intergranular diffusion

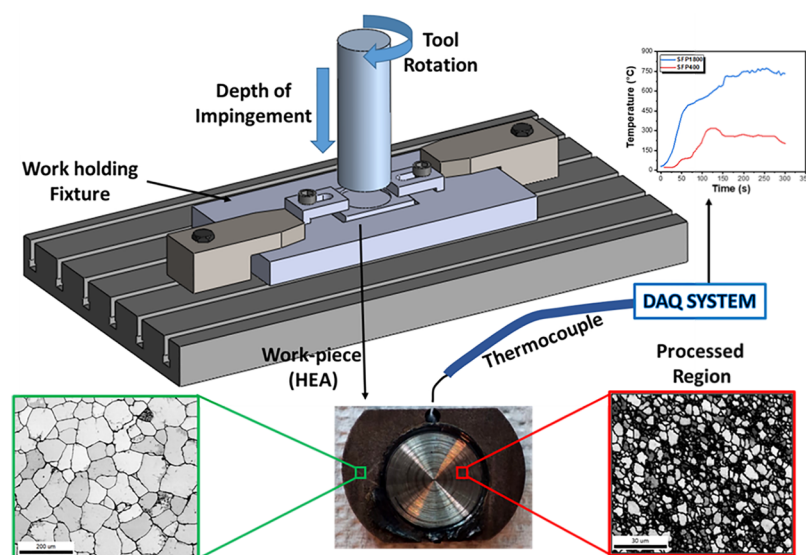


Figure 12. Schematic representation of stationary friction processing (SFP).

of mobile atoms owing to high number of GBs, which would accelerate the formation of a continuous layer due to the high diffusivity of ionic species.³⁶ High density GBs facilitate rapid oxidation of chromium cations and form continuous chromia protective scales, which limit the oxidation kinetics over a period of time.

3. CONCLUSION

A coarse grain microstructure having BCC/B2 phases was obtained in the as-cast HEA sample. Only 5 min of straining of sample significantly refined the grain structure from 98 to 1 μm and 0.43 μm for the SFP_400 and SFP_1800 sample, respectively. The ultrafine-grained samples showed a phase transition from BCC/B2 to FCC structure. The SFP_400 sample showed a 12–20% reduction in the oxidation kinetics, whereas the SFP_1800 sample showed a 38–48% reduction in the oxidation kinetics compared to the as-cast alloy. Low values of parabolic rate constant and high values of activation energy for the ultrafine-grained samples show the high oxidation resistance of the processed samples. Protective oxide scales of Al_2O_3 and Cr_2O_3 were predominantly found after discontinuous isothermal oxidation. Other than protective scales, the availability of $\text{Co}(\text{Cr,Fe})_2\text{O}_4$ spinel phases was also observed during the oxidation at elevated temperatures. The presence of more GBs favoring outward flux of elements to form a dense chromia layer followed by internal Al-rich oxide layered structure is responsible for the enhanced oxidation resistance of the processed samples.

4. EXPERIMENTAL DETAILS

Al, Co, Cr, Fe, and Ni (99.99% purity) elements were used to prepare the equimolar AlCoCrFeNi HEA in an arc melting furnace. A sample of dimensions $20 \times 15 \times 2 \text{ mm}^3$ was sectioned and used for stationary friction processing (SFP). In SFP, a WC-cylindrical tool of 12 mm diameter was rotated and inserted into the work piece. The tool was kept rotating at a fixed location at two different rotational speeds, 400 and 1800 rpm, for 5 min. A data acquisition system (DAQ) equipped with a K-type thermocouple was utilized for the temperature measurement during processing. A schematic illustration of SFP is shown in Figure 12. The circular processed section of

10 mm diameter was sectioned from the sample. As-cast and processed samples were polished up to 2000 grit paper and ultrasonically cleaned in ethanol. The tubular furnace was set to three different temperatures, 850, 950, and 1050 $^\circ\text{C}$, with a heating rate of 10 $^\circ\text{C}/\text{min}$ and dwell time of 100 h. All three samples were exposed to high temperature oxidation after reaching the set temperature in the presence of laboratory air. Mass gain of each sample was measured after every 5 h until 50 h followed by after every 10 h until 100 h. The mass gain measurements were performed using a high precision weighing scale with a least count of 0.01 mg. Before oxidation, the cross section of the processed sample was polished and etched in aqua-regia solution for 20 s to reveal the depth of refinement (DOR) using optical microscopy (Leica DM750M, Germany). Contact angle measurements were performed using a goniometer (Apex Instruments, India) by the sessile drop method to estimate the surface free energy of the samples before oxidation. The samples that were 2000-grit paper polished, followed by vibromet polishing in colloidal silica, were used for contact angle measurement. Five drops were dropped on each sample, and the average of the five values was calculated. Also, X-ray diffraction (XRD) (Bruker, D8 Discover) and EBSD (FEI Quanta 3D FEG) measurements were performed on the surface of as-cast and processed samples. XRD analysis was performed in a 2θ range of 20° – 100° with a step size of 0.01313° and scan rate $0.02^\circ/\text{s}$ using a $\text{Cu K}\alpha$ source of radiation ($\lambda = 1.54 \text{ \AA}$) in reflection type (Bragg–Brentano geometry) configuration. XRD, scanning electron microscopy (SEM) (JEOL JSM-7610F Plus) and energy dispersive X-ray spectroscopy (EDS) (EDAX AMETEK) analyses were performed on the oxidation products of the HEA samples. X'Pert HighScore Plus software was used to quantify the oxide phases in the XRD spectra. The accelerating voltage and probe current used for SEM imaging were 15 kV and 80 pA, while these values for EDS and EBSD mapping were 20 kV and 450 pA.

■ ASSOCIATED CONTENT

SI Supporting Information

The Supporting Information is available free of charge at <https://pubs.acs.org/doi/10.1021/acsomega.1c06014>.

Temperature profile during SFP, fitting of grain size distribution of processed samples, EBSD phase maps, W–H plot, residual stress curve, 3D surface profiles, scale thickness measurement, and oxide contribution details (PDF)

AUTHOR INFORMATION

Corresponding Author

Harpreet S. Arora – Surface Science and Tribology Lab,
Department of Mechanical Engineering, Shiv Nadar
University, Greater Noida, Uttar Pradesh 201314, India;
orcid.org/0000-0002-5674-2930;
Email: harpreet.arora@snu.edu.in

Authors

Mayank Garg – Surface Science and Tribology Lab,
Department of Mechanical Engineering, Shiv Nadar
University, Greater Noida, Uttar Pradesh 201314, India;
orcid.org/0000-0002-4958-7784

Harpreet S. Grewal – Surface Science and Tribology Lab,
Department of Mechanical Engineering, Shiv Nadar
University, Greater Noida, Uttar Pradesh 201314, India;
orcid.org/0000-0001-9265-4674

Ram K. Sharma – Centre for Inter-Disciplinary Research and
Innovation, University of Petroleum and Energy Studies,
Dehradun, Uttarakhand 248007, India

Complete contact information is available at:

<https://pubs.acs.org/10.1021/acsomega.1c06014>

Notes

The authors declare no competing financial interest.

REFERENCES

- (1) (a) Akella, A. K.; Saini, R. P.; Sharma, M. P. Social, economical and environmental impacts of renewable energy systems. *Renew. Energy* **2009**, *34* (2), 390–396. (b) IEA *Electricity Information 2019*; OECD Publishing, 2019.
- (2) Yonezawa, K.; Nakai, G.; Takayasu, M.; Sugiyama, K.; Sugita, K.; Umezawa, S.; Ohmori, S. Influence of blade corrosion on aerodynamic characteristics of a gas turbine. *Energy* **2021**, *230*, 120665.
- (3) Zhang, T. Methods of Improving the Efficiency of Thermal Power Plants. *J. Phys. Conf. Ser.* **2020**, *1449*, 012001.
- (4) (a) Li, S.; Smith, D. High temperature fatigue-creep behaviour of single crystal SRR99 nickel base SUPERALLOYS: part ii—fatigue-creep life behaviour. *Fatigue Fract. Eng. Mater. Struct.* **1995**, *18* (5), 631–643. (b) Pieraggi, B. Effect of creep or low cycle fatigue on the oxidation or hot corrosion behaviour of nickel-base superalloys. *Mater. Sci. Eng.* **1987**, *88*, 199–204.
- (5) Rhys-Jones, T.; Toriz, F. Thermal barrier coatings for turbine applications in aero engines. *High Temp. Technol.* **1989**, *7* (2), 73–81.
- (6) (a) Chen, J.; Niu, P.; Liu, Y.; Lu, Y.; Wang, X.; Peng, Y.; Liu, J. Effect of Zr content on microstructure and mechanical properties of AlCoCrFeNi high entropy alloy. *Mater. Des.* **2016**, *94*, 39–44. (b) Munitz, A.; Salhov, S.; Hayun, S.; Frage, N. Heat treatment impacts the micro-structure and mechanical properties of AlCoCrFeNi high entropy alloy. *J. Alloys Compd.* **2016**, *683*, 221–230. (c) Wang, F.; Zhang, Y.; Chen, G.; Davies, H. Cooling rate and size effect on the microstructure and mechanical properties of AlCoCrFeNi high entropy alloy. *J. Eng. Mater. Technol.* **2009**, *131* (3), 034501. (d) Wu, Z.; Bei, H.; Pharr, G. M.; George, E. P. Temperature dependence of the mechanical properties of equiatomic solid solution alloys with face-centered cubic crystal structures. *Acta Mater.* **2014**, *81*, 428–441.
- (7) Shivam, V.; Shadangi, Y.; Basu, J.; Mukhopadhyay, N. J. J. o. A. *Compounds. Evolution of phases, hardness and magnetic properties of AlCoCrFeNi high entropy alloy processed by mechanical alloying* **2020**, *832*, 154826.
- (8) (a) Wang, Y.; Yang, Y.; Yang, H.; Zhang, M.; Ma, S.; Qiao, J. Microstructure and wear properties of nitrided AlCoCrFeNi high-entropy alloy. *Mater. Chem. Phys.* **2018**, *210*, 233–239. (b) Wang, Z.; Qiu, W.; Yang, Y.; Liu, C. Atomic-size and lattice-distortion effects in newly developed high-entropy alloys with multiple principal elements. *Intermetallics* **2015**, *64*, 63–69.
- (9) Hemphill, M. A.; Yuan, T.; Wang, G.; Yeh, J.; Tsai, C.; Chuang, A.; Liaw, P. Fatigue behavior of Al_{0.5}CoCrCuFeNi high entropy alloys. *Acta Mater.* **2012**, *60* (16), 5723–5734.
- (10) (a) Raphel, A.; Kumaran, S.; Kumar, K. V.; Varghese, L. Oxidation and corrosion resistance of AlCoCrFeTiHigh entropy alloy. *Mater. Today: Proc.* **2017**, *4* (2), 195–202. (b) Yen, C.-C.; Lu, H.-N.; Tsai, M.-H.; Wu, B.-W.; Lo, Y.-C.; Wang, C.-C.; Chang, S.-Y.; Yen, S.-K. J. C. S. *Corrosion mechanism of annealed equiatomic AlCoCrFeNi tri-phase high-entropy alloy in 0.5 M H₂SO₄ aerated aqueous solution* **2019**, *157*, 462–471.
- (11) Kim, Y.-K.; Joo, Y.-A.; Kim, H. S.; Lee, K.-A. High temperature oxidation behavior of Cr-Mn-Fe-Co-Ni high entropy alloy. *Intermetallics* **2018**, *98*, 45–53.
- (12) Nong, Z.-S.; Lei, Y.-N.; Zhu, J.-C. Wear and oxidation resistances of AlCrFeNiTi-based high entropy alloys. *Intermetallics* **2018**, *101*, 144–151.
- (13) Chen, L.; Zhou, Z.; Tan, Z.; He, D.; Bobzin, K.; Zhao, L.; Öte, M.; Königstein, T. High temperature oxidation behavior of Al_{0.6}CrFeCoNi and Al_{0.6}CrFeCoNiSi_{0.3} high entropy alloys. *J. Alloys Compd.* **2018**, *764*, 845–852.
- (14) Lu, J.; Chen, Y.; Zhang, H.; Li, L.; Fu, L.; Zhao, X.; Guo, F.; Xiao, P. Effect of Al content on the oxidation behavior of Y/Hf-doped AlCoCrFeNi high-entropy alloy. *Corros. Sci.* **2020**, *170*, 108691.
- (15) Wen, M.; Wen, C.; Hodgson, P.; Li, Y. J. C. s. *Thermal oxidation behaviour of bulk titanium with nanocrystalline surface layer* **2012**, *59*, 352–359.
- (16) Kanjer, A.; Optasanu, V.; Marco de Lucas, M.C.; Heintz, O.; Geoffroy, N.; Francois, M.; Berger, P.; Montesin, T.; Lavis, L. Improving the high temperature oxidation resistance of pure titanium by shot-peening treatments. *Surf. Coat. Technol.* **2018**, *343*, 93–100.
- (17) Garg, M.; Grewal, H. S.; Arora, H. S. Effect of microwave processing on the oxidation behavior of refractory high entropy alloy. *Mater. Chem. Phys.* **2021**, *262*, 124256.
- (18) Liu, J.; Suslov, S.; Li, S.; Qin, H.; Ren, Z.; Ma, C.; Wang, G.-X.; Doll, G. L.; Cong, H.; Dong, Y.; Ye, C. Effects of ultrasonic nanocrystal surface modification on the thermal oxidation behavior of Ti6Al4V. *Surf. Coat. Technol.* **2017**, *325*, 289–298.
- (19) Benafia, S.; Retraint, D.; Yapi Brou, S.; Panicaud, B.; Grosseau Poussard, J.L. Influence of surface mechanical attrition treatment on the oxidation behaviour of 316L stainless steel. *Corros. Sci.* **2018**, *136*, 188–200.
- (20) Khanna, A.; Gnanamoorthy, J. Effect of cold work on the oxidation resistance of $\frac{1}{4}$ Cr-1 Mo steel. *Oxid. Met.* **1985**, *23* (1), 17–33.
- (21) (a) Arora, H. S.; Ayyagari, A.; Saini, J.; Selvam, K.; Riyadh, S.; Pole, M.; Grewal, H. S.; Mukherjee, S. High Tensile Ductility and Strength in Dual-phase Bimodal Steel through Stationary Friction Stir Processing. *Sci. Rep.* **2019**, *9* (1), 1972. (b) Selvam, K.; Saini, J.; Perumal, G.; Ayyagari, A.; Salloom, R.; Mondal, R.; Mukherjee, S.; Grewal, H. S.; Arora, H. S. Exceptional cavitation erosion-corrosion behavior of dual-phase bimodal structure in austenitic stainless steel. *Tribol. Int.* **2019**, *134*, 77–86.
- (22) Chang, C. I.; Lee, C. J.; Huang, J. C. Relationship between grain size and Zener–Holloman parameter during friction stir processing in AZ31 Mg alloys. *Scr. Mater.* **2004**, *51* (6), 509–514.
- (23) Selvam, K.; B S, R.; Grewal, H. S.; Arora, H. S.; Singh, H. High strain deformation of austenitic steel for enhancing erosion resistance. *Wear* **2017**, *376–377*, 1021–1029.

- (24) (a) Bahramyan, M.; Mousavian, R. T.; Brabazon, D. Study of the plastic deformation mechanism of TRIP–TWIP high entropy alloys at the atomic level. *Int. J. Plast.* **2020**, *127*, 102649. (b) Ojha, A.; Sehitoglu, H. Transformation stress modeling in new FeMnAlNi shape memory alloy. *Int. J. Plast.* **2016**, *86*, 93–111. (c) Zhang, T.; Zhao, R.; Wu, F.; Lin, S.; Jiang, S.; Huang, Y.; Chen, S.; Eckert, J. Transformation-enhanced strength and ductility in a FeCoCrNiMn dual phase high-entropy alloy. *Mater. Sci. Eng., A* **2020**, *780*, 139182.
- (25) Biju, V.; Sugathan, N.; Vrinda, V.; Salini, S. L. Estimation of lattice strain in nanocrystalline silver from X-ray diffraction line broadening. *J. Mater. Sci.* **2008**, *43* (4), 1175–1179.
- (26) Fowkes, F. M. Attractive forces at interfaces. *Ind. Eng. Chem. Res.* **1964**, *56* (12), 40–52.
- (27) Jańczuk, B.; Biallopiotrowicz, T. Surface free-energy components of liquids and low energy solids and contact angles. *J. Colloid Interface Sci.* **1989**, *127* (1), 189–204.
- (28) Wu, S. *Polymer interface and adhesion*; Routledge, 2017.
- (29) Van Oss, C. J. *Interfacial forces in aqueous media*; CRC Press, 2006.
- (30) Kofstad, P. Oxidation of metals: determination of activation energies. *Nature* **1957**, *179* (4574), 1362–1363.
- (31) (a) Butler, T. M.; Weaver, M. L. Oxidation behavior of arc melted AlCoCrFeNi multi-component high-entropy alloys. *J. Alloys Compd.* **2016**, *674*, 229–244. (b) Zhao, S.; Xie, X.; Smith, G. D. The oxidation behavior of the new nickel-based superalloy Inconel 740 with and without Na₂SO₄ deposit. *Surf. Coat. Technol.* **2004**, *185* (2–3), 178–183.
- (32) Birks, N.; Meier, G. H.; Pettit, F. S. *Introduction to the High Temperature Oxidation of Metals*; Cambridge University Press, 2006; DOI: 10.1017/CBO9781139163903.
- (33) (a) Chen, Y.; Zhao, X.; Xiao, P. Effect of microstructure on early oxidation of MCrAlY coatings. *Acta Mater.* **2018**, *159*, 150–162. (b) Lu, J.; Li, L.; Chen, Y.; Liu, X.; Zhao, X.; Guo, F.; Xiao, P. Y-Hf co-doped AlCoCrFeNi high-entropy alloy coating with superior oxidation and spallation resistance at 1100° C. *Corros. Sci.* **2021**, *182*, 109267.
- (34) Peng, X.; Yan, J.; Zhou, Y.; Wang, F. Effect of grain refinement on the resistance of 304 stainless steel to breakaway oxidation in wet air. *Acta Mater.* **2005**, *53* (19), 5079–5088.
- (35) (a) Jayaraj, J.; Thirathipviwat, P.; Han, J.; Gebert, A. Microstructure, mechanical and thermal oxidation behavior of AlNbTiZr high entropy alloy. *Intermetallics* **2018**, *100*, 9–19. (b) Senkov, O.; Senkova, S.; Dimiduk, D.; Woodward, C.; Miracle, D. J. J. o. M. S. *Oxidation behavior of a refractory NbCrMo 0.5 Ta 0.5 TiZr alloy* **2012**, *47* (18), 6522–6534. (c) Sheikh, S.; Bijaksana, M. K.; Motallebzadeh, A.; Shafeie, S.; Lozinko, A.; Gan, L.; Tsao, T.-K.; Klement, U.; Canadinc, D.; Murakami, H.; Guo, S. Accelerated oxidation in ductile refractory high-entropy alloys. *Intermetallics* **2018**, *97*, 58–66.
- (36) Wang, Y.; Zhang, M.; Jin, J.; Gong, P.; Wang, X. Oxidation behavior of CoCrFeMnNi high entropy alloy after plastic deformation. *Corros. Sci.* **2020**, *163*, 108285.